3162 Chem. Mater. **2009,** *21,* 3162–3176
DOI:10.1021/cm900581b

CHEMISTRY OF MATERIALS
Article

Investigation of the Conversion Reaction Mechanisms for Binary Copper(II) Compounds by Solid-State NMR Spectroscopy and X-ray Diffraction

Naoko Yamakawa,[†,‡] Meng Jiang,[†] and Clare P. Grey*[,†]

[†] *Department of Chemistry, SUNY Stony Brook, Stony Brook, New York 11794-3400, and* [‡] *Energy Research & Development Division, Chemical & Energy Business Group, Sony Corporation, 1-1 Aza, Shimosugishita, Takakura, Hiwada-machi, Koriyama-shi, Fukushima, 963-0531 Japan*

Received February 27, 2009. Revised Manuscript Received June 2, 2009

The conversion reaction mechanisms of CuS, CuF_2, and CuO during the electrochemical reaction with Li are studied by solid-state ^{63}Cu, ^{19}F, and ^{7}Li nuclear magnetic resonance (NMR) and X-ray diffraction (XRD). For CuS, a two-step reaction is observed that is associated with an insertion reaction involving first limited incorporation of Li into CuS and then a two-phase reaction to form a material with the approximate composition LiCuS. This is followed by a conversion reaction to form Li_2S and Cu, $Cu_{1.96}S$ being formed as a side product of the decomposition of LiCuS. Evidence for the insertion phases is found from both NMR and XRD. A direct conversion reaction to form LiF and Cu is seen for CuF_2, whereas the ^{7}Li NMR results indicate that CuO can tolerate a small amount of Li substitution before reacting to form Li_2O and Cu. Both the diffraction and NMR results indicate that the size of the Cu particles formed on discharge are much larger in the CuS system, which is thought to result from the higher Cu^{1+} mobilities in the intermediate intercalation compounds Li_xCuS. The factors that control the possible mechanisms for these conversion reactions are discussed.

1. Introduction

Lithium ion batteries, as one of the most important rechargeable energy storage technologies, have received much recent attention. They have been widely used for various mobile equipment including cell phones, laptop computers, and power tools. They are also promising candidates as power sources for automotive applications. Although intensive research has been done to improve the performance of Li ion batteries, there are still many remaining challenges to be overcome so that they can be used in a wider range of applications. In particular, cheaper and safer electrodes are required with much higher reversible capacity.[1] Graphite and carbonaceous materials represent the main commercial anode materials with specific capacities of ~372 mA h/g.[2,3] These materials operate by reversible intercalation of Li between the carbon layers. A significant advance in the field came with the discovery of materials that operate via a so-called "conversion mechanism". This was first demonstrated by Y. Idota et al. in 1997, where a tin-based amorphous oxide was used as the anode material in a Li ion battery, the reaction mechanism relying on the formation of metal particles surrounded by an oxide phase.[4−6] 3d-transition metal compounds M_xX_y (M=Co, Fe, Ni, Cu, etc.; X=F, O, S, N, etc.) have now been widely investigated for their potential use in lithium batteries because of their high capacities. Because the various compounds have different voltage windows, they can have potential applications as either cathodes or anodes and Tarascon and co-workers have demonstrated that they can have specific capacities of as high as 600−1000 mA h/g with good cycling reversibility.[7] The conversion reaction mechanism can be written as follows

$$M_xX_y + nyLi \Leftrightarrow yLi_nX + xM \quad (1)$$

In these reactions, usually micrometer-size metal oxides or binary compounds react to form nanosized metal and Li_nX particles in the range of 1−10 nm in the first reduction reaction. The size of the particles remains essentially unchanged in the following cycles, the electrochemically driven nanosize confinement of the metal particles being thought to enhance their electrochemical reaction activity. Though these 3d-transition metal compounds have unique electrochemical characteristics, the size of the particles formed in these processes hinders an understanding of all the details of these mechanisms, including the structure of any intermediate phases that form during the conversion reactions, and prevents optimization of these electrode systems.

---

*Corresponding author. E-mail: cgrey@notes.cc.sunysb.edu.

(1) Tarascon, J. M.; Armand, M. *Nature* **2001**, *414*(6861), 359–367.

(2) Dahn, J. R.; Zheng, T.; Liu, Y. H.; Xue, J. S. *Science* **1995**, *270* (5236), 590–593.

(3) Megahed, S.; Scrosati, B. *J. Power Sources* **1994**, *51*(1−2), 79–104.

(4) Courtney, I. A.; Dahn, J. R. *J. Electrochem. Soc.* **1997**, *144*(9), 2943–2948.

(5) Courtney, I. A.; Dahn, J. R. *J. Electrochem. Soc.* **1997**, *144*(6), 2045–2052.

(6) Idota, Y.; Kubota, T.; Matsufuji, A.; Maekawa, Y.; Miyasaka, T. *Science* **1997**, *276*(5317), 1395–1397.

(7) Poizot, P.; Laruelle, S.; Grugeon, S.; Dupont, L.; Tarascon, J. M. *Nature* **2000**, *407*(6803), 496–499.

The work presented in this paper uses solid-state magic angle spinning (MAS) nuclear magnetic resonance (NMR) to study the conversion/reconversion reaction mechanisms, with supporting evidence from high resolution X-ray diffraction (XRD). In this study, three Cu compounds CuF_2, CuS and CuO are chosen as model transition metal binary compounds, since their magnetic properties make them more amenable to NMR studies than many other transition metals: transition metal particles are generated in the conversion reaction, and unlike other metals such as cobalt, iron, and nickel, copper metal is not ferromagnetic.

Of the three copper compounds, CuF_2 is the most attractive cathode material because it has the highest theoretical potential of 3.55 V based on thermodynamic calculations[8,9] and a specific capacity of 528 mA h/g. Practical utilization of this compound at an appropriate voltage has proven difficult, in part because of the hydrated impurities often found together with this phase and problems due to Cu dissolution. In addition, like many fluorides, CuF_2 is an insulator. To overcome the last problem, Badway et al. have proposed the use of a mixed conductive matrix (MCM) and have demonstrated a full utilization of this material by using carbon and/or a conducting oxides such as MoO_3, etc.[10] The improved properties have been ascribed to both (i) a drastic reduction of particle size, which shortens the tunneling lengths for the electrons and increases the interface for reaction with Li, and (ii) the presence of conductive materials connecting each nanograin.

CuS is also a promising cathode material for use in a low voltage battery system, due to its high specific capacity of 561 mA h/g and good electronic conductivity of 1×10^{-3} Scm^{-1}.[11−13] There are two voltage regions in the CuS discharge profile, one at approximately 2.05 V and the other at 1.68 V, which according to Chung et al.[14] correspond to the following reactions

$$CuS + xLi^+ + xe^- \rightarrow Li_xCuS \quad \text{(first process)} \tag{2}$$

$$1.96Li_xCuS + (2-1.96x)Li^+ + (2-1.96x)e^- \rightarrow Li_2S + Cu_{1.96}S \tag{3}$$

$$Cu_{1.96}S + 2Li^+ + 2e^- \rightarrow Li_2S + 1.96Cu \quad \text{(second process)} \tag{4}$$

The first process comprises an insertion reaction, the product of the insertion reaction Li_xCuS then reacting with more Li to generate $Cu_{1.96}S$ and Li_2S. Subsequently, a plateau is observed, involving the conversion of $Cu_{1.96}S$ to Li_2S and copper metal. In contrast, Debart et al. proposed that Cu_2S is formed as the intermediate phase, which then transforms into Cu and Li_2S, as described as follows[15]

$$CuS + e^- + Li^+ \rightarrow \frac{1}{2}Cu_2S + \frac{1}{2}Li_2S \tag{5}$$

$$\frac{1}{2}Cu_2S + e^- + Li^+ \rightarrow \frac{1}{2}Li_2S + Cu \tag{6}$$

The final material investigated here, CuO, has a specific capacity of 674 mA h/g and several discharge reaction mechanisms have been also proposed by X-ray analysis for this material.[16−19]

In this paper, we compare the effect of three different anions (F^-, S^{2-} and O^{2-}) on conversion reactions involving copper. The electrochemistry of all the materials is first presented, and the high-resolution X-ray diffraction (XRD) data and ^7Li, ^{63}Cu, and ^{19}F NMR spectra for each compound are then analyzed individually. The redox reaction mechanisms and the different electrochemical performances of the three compounds are then compared. We demonstrate that NMR spectroscopy can be used to detect insertion phases and Li_nX phases that are not readily observed by XRD and that it is extremely sensitive to the size of the copper particles formed on discharge.

2. Experimental Section

2.1. Materials Preparation. Commercial CuS (Kojundo Chemical Laboratory) and CuO (Kanto Chemical Co.) were used in this study without further treatment. For CuF_2, carbon-coated nano-CuF_2 (CCN-CuF_2) was prepared by high energy ball milling of CuF_2 (Kojundo Chemical Laboratory) with carbon black (Ketjen Black International Company). Stoichiometric mixtures (CuF_2:carbon black = 80:20 wt %) were placed inside a steel milling cell (Rotec) with zirconium balls. The milling was performed for 3 h with 500 rpm.

2.2. Electrochemical Characterization. The cathodes were prepared by mixing 80 wt % CuS, CuO, or CCN-CuF_2, 15 wt % graphite as an electronic conductor, and 5 wt % polyvinylidene fluoride (PVDF) as a binder in *N*-methylpyrrolidinone. The slurry was coated on aluminum foil and dried at 100 °C until the solvent had evaporated completely. Coin type (2032) cells were assembled in an argon-filled glovebox with Li metal foil (Aldrich) as the anode, polypropylene separators (Celgard) and 1 M solution of $LiPF_6$ in EC (ethylene carbonate): DMC (dimethyl carbonate)=1:1 as the electrolyte. Swagelok type cells were also assembled with a mixture of 85 wt % CuS, CuO, or CCN-CuF_2 and 15 wt % carbonblack as the cathode and Whatman GF/D fiber as separator. The other components are the same as used in the coin cells. Note that because the CCN-CuF_2 nanocomposite comprises 20 wt % carbon, the coin and swagelok cells contain 64 and 68 wt % active material, respectively.

---

(8) Li, H.; Balaya, P.; Maier, J. *J. Electrochem. Soc.* **2004**, *151*(11), A1878–A1885.

(9) Li, H.; Richter, G.; Maier, J. *Adv. Mater.* **2003**, *15*(9), 736–739.

(10) Badway, F.; Mansour, A. N.; Pereira, N.; Al-Sharab, J. F.; Cosandey, F.; Plitz, I.; Amatucci, G. G. *Chem. Mater.* **2007**, *19* (17), 4129–4141.

(11) Gabano, J. P.; Gerbier, G.; Jammet, J.; Dechenau,V, J. Electrochem. Soc. **1972**, *119*, (4), 459−461.

(12) Okamoto, K.; Kawai, S. *Jpn. J. Appl. Phys.* **1973**, *12*(8), 1130–1138.

(13) Etienne, A. *J. Electrochem. Soc.* **1970**, *117*(7), 870–874.

(14) Chung, J. S.; Sohn, H. J. *J. Power Sources* **2002**, *108*(1−2), 226–231.

(15) Debart, A.; Dupont, L.; Patrice, R.; Tarascon, J. M. *Solid State Sci.* **2006**, *8*(6), 640–651.

(16) Grugeon, S.; Laruelle, S.; Herrera-Urbina, R.; Dupont, L.; Poizot, P.; Tarascon, J. M. *J. Electrochem. Soc.* **2001**, *148*(4), A285–A292.

(17) Ikeda, H.; Narukawa, S. *J. Power Sources* **1983**, *9*(3−4), 329–334.

(18) Matsuda, Y.; Teraji, K.; Takasu, Y. *Denki Kagaku* **1976**, *44*(5), 363–364.

(19) Novak, P. *Electrochim. Acta* **1985**, *30*(12), 1687–1692.

Electrochemical experiments were carried out on a battery cycler (Arbin Instruments, College Station, Texas) in galvanostatic mode at a *C*/35 rate, between 1.0 and 3.0 V. The Li content in each cycled sample is calculated from the capacity, assuming 100% columbic efficiency. Galvanostatic intermittent titration (GITT) experiments were performed for CuS at *C*/35 rate with 1 h current step and a rest period of 12 h.

2.3. X-ray Diffraction. X-ray diffraction (XRD) was used to confirm the structure of the CCN-CuF_2 and study the phase transitions that occur during the electrochemical processes. Laboratory XRD was performed on a Rigaku powder X-ray diffractometer equipped with a Cr target X-ray tube (Cr $K\alpha_1$: $\lambda = 2.2898$ Å). A range of 2θ values from 20 to 120°, with a scanning rate of 1° per minute and a step size of 0.02°, 2θ were used. High resolution (HR)-XRD was carried out at the 11-BM beamline at the Advanced Photon Source (APS) in Argonne National Laboratory ($\lambda = 0.4001$ Å),[20,21] and at the X16C beamline at National Synchrotron Light Source (NSLS) in Brookhaven National Laboratory ($\lambda = 0.6881$ Å). Ex situ XRD was accomplished by disassembling the Swagelok type cells in an argon-filled glovebox after batteries had been cycled to the desired voltages. If it is not specified, the XRD data shown in this paper were collected at 11-BM beamline at the APS.

2.4. MAS NMR Spectroscopy. ^{7}Li MAS NMR spectroscopy was performed on cycled CuS, CuO and CCN-CuF_2 samples with a 1.8 mm probe on a CMX-200 spectrometer using a magnetic field strength of 4.7 T. A spinning frequency of 38 kHz and a rotor-synchronized spin−echo sequence (90°−τ−180°−τ−acq) were used to acquire the spectra. The spectra were collected at an operating frequency of 77.10 MHz. $\pi/2$ pulses of 2.5 μs were used, with a delay time of 1.0 s. For better resolution, ^{7}Li NMR spectra of cycled CuS samples were also acquired on a Varian InfinityPlus-360 spectrometer with a magnetic field strength of 8.47T. A 4 mm HXY probe with a pulse width 3.25 μs and a pulse delay 10 s at a 10 kHz spinning speed were used. All the spectra were referenced to 1 M ^{7}LiCl (in H_2O) at 0 ppm.

^{19}F MAS NMR spectroscopy was performed on discharged CCN-CuF_2 samples with a 3.2 mm probe on the Varian InfinityPlus-360 at an operating frequency of 338.73 MHz. A spinning speed of 20 kHz and a rotor-synchronized spin−echo sequence (90°−τ−180°−τ−acq) were used to acquire the spectra. A $\pi/2$ pulse of 5.75 μs was used, with a delay time of 1.0 s. The spectra were referenced to fluorobenzene (MFB) at −113.8 ppm.[22]

^{63}Cu MAS NMR spectroscopy was performed with a 4 mm HXY probe on both the Varian InfinityPlus-360 and CMX-200 spectrometers at operating frequencies of 95.53 and 53.07 MHz, respectively. A spinning speed of 10 kHz and a rotor-synchronized spin−echo sequence (90°−τ−180°−τ−acq) were used to acquire the spectra. 90° pulses of 5.0 μs at 8.46 T and 3.25 μs at 4.7 T were used, with a delay time of 1.0 s. The static ^{63}Cu NMR spectra were performed with a static probe with silver coil on the CMX-200 spectrometer. A one pulse sequence with a $\pi/2$ of 2.0 μs was used with a delay time of 1.0 s. The spectra were referenced to solid CuCl at −319 ppm.[23]

Unless otherwise stated, all the ^{7}Li, ^{19}F, and ^{63}Cu data are plotted in absolute intensity mode, i.e., all the spectra have been normalized, taking into account the number of data acquisitions and the mass of the samples. Although changes in probe tuning, particularly in samples containing metals, may result in small changes in spectral sensitivity, and differences in spin−spin relaxation (T_2) may affect the relative intensities of the resonances in Hahn echo experiments, the intensity of the spectra provides an approximate estimate of the concentration of observable nuclei.

3. Results

3.1. Pristine CCN-CuF_2 Characterization. To examine the effect of ball-milling, we performed X-ray diffraction on the CCN-CuF_2 sample (Figure 1). After the milling treatment, significant broadening of the Bragg peaks was observed, and the crystalline size, as determined by the Scherrer formula[24] by using the (011) Bragg peak for CCN-CuF_2, was ~16 nm. No extra peaks were observed, indicating that no crystalline impurities are introduced during milling and that the structure remains unchanged.

3.2. Electrochemical Characterization. The electrochemical performances of CCN-CuF_2, CuS and CuO were investigated in a voltage window between 3.0 and 1.0 V (vs Li/Li^+) at room temperature at a *C*/35 rate (Figure 2a−c). The discharge profile of CCN-CuF_2 shows a plateau at 3.0 V from Li = 0 to 1.0 and then the voltage drops slowly reaching approximately 1.0 V at Li = 2.1. A very similar profile was observed for a cell discharged at the slower rate of *C*/100. A slight drop and then recovery of the potential is seen at the beginning of the discharge, suggesting that a new phase is nucleating. A specific capacity of 566 mAh/g is achieved on discharge, which is slightly above the theoretical capacity of 528 mA h/g. This is ascribed to electrolyte decomposition and solid−electrolyte interface (SEI) formation at low voltages and the onset of the reaction with carbon. Li et al. also observed additional capacity, which they have ascribed to a space-charge storage mechanism.[8] However, most of this additional capacity was seen below 1.01 V. Negligible capacity is observed on charge.

The discharge profile of CuS shows two apparent plateaus, one at 2.05 V and the other one at 1.68 V. The capacities from the first and the second plateau (including the voltage drop at the end) are 240 and 231 mA h/g, which correspond to Li0.85 and Li0.82, respectively. The total capacity, 471 mA h/g (Li1.7), is only 85% of the theoretical capacity of 561 mA h/g. On charge, the curve shows quite different features from those seen on discharge. The charge capacity is 377 mA h/g, which corresponds to 79% of the discharge capacity and 100 mA h/g (Li0.35) is not recovered. Figure 2d shows the GITT profile of CuS. A gradual decrease of the equilibrium voltage is observed until approximately Li0.16, and then the voltage remains constant at 2.1 V on the first plateau until approximately Li0.85, and then at 1.81 V (the second plateau) until the end of

---

(20) Lee, P. L.; Shu, D. M.; Ramanathan, M.; Preissner, C.; Wang, J.; Beno, M. A.; Von Dreele, R. B.; Ribaud, L.; Kurtz, C.; Antao, S. M.; Jiao, X.; Toby, B. H. *J. Synchrotron Radiat.* **2008**, *15*, 427–432.

(21) Wang, J.; Toby, B.H.; Lee, P.L.; Ribaud, L.; Antao, S.M.; Kurtz, C.; Ramanathan, M.; Von Dreele, R.B.; Beno, M.A. *Rev. Sci. Instrum.* **2008**, *79*, 085105.

(22) Hinedi, Z. R.; Chang, A. C.; Borchardt, D. B. *Water Res.* **1997**, *31* (4), 877–883.

(23) Liu, H. M.; Sullivan, R. M.; Hanson, J. C.; Grey, C. P.; Martin, J. D. *J. Am. Chem. Soc.* **2001**, *123*(31), 7564–7573.

(24) West, A. R. *Solid State Chemistry and Its Application*; John Wiley & Sons: New York: 1992.

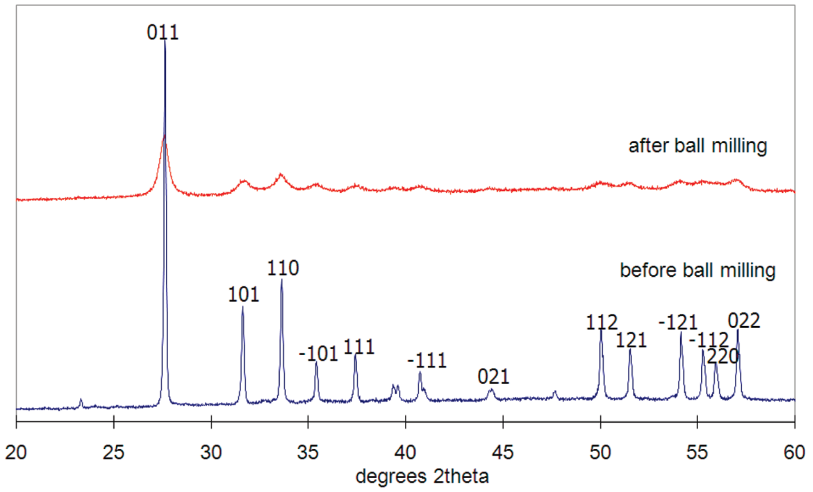

Figure 1. XRD pattern of CCN-CuF_2 prepared by high energy ball milling. The more intense reflections (indexed with a P_{21}/c space group) are labeled.

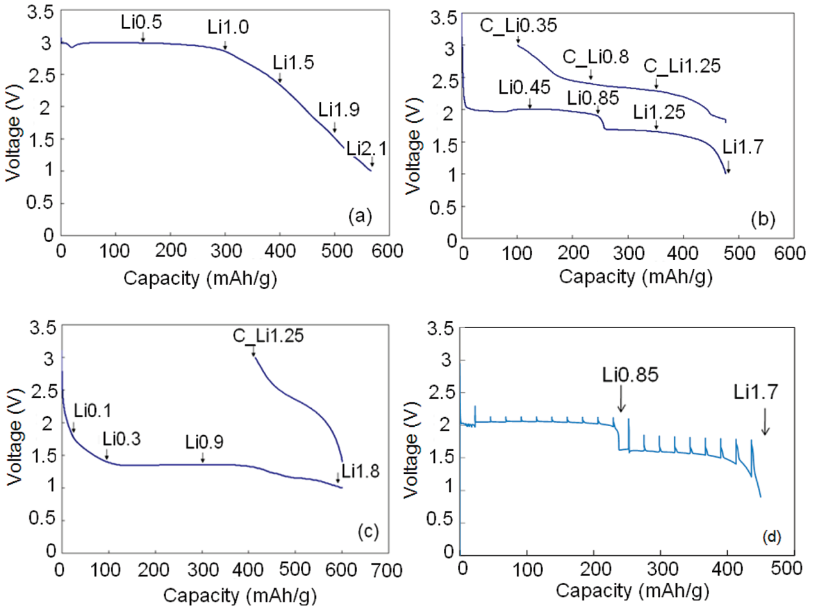

Figure 2. Electrochemical curves of (a) CCN-CuF_2, (b) CuS, (c) CuO cycled at room temperature at $C/35$. (d) Galvanostatic intermittent titration (GITT) results for CuS. The compositions of the different samples prepared as part of this study are indicated with arrows. The Li content (Lix) in each sample is calculated from the discharge capacity in this and subsequent figures and assumes 100% Coulombic efficiency.

discharge. This is consistent with the two processes observed in the galvanostatic profile. The step size used in this experiment was too large to allow for a more detailed characterization of the beginning of the discharge process. However, it does indicate that process from Li0 to Li0.16 is different from the process occurring from Li0.16 to Li0.85, and suggests that CuS may be able to accommodate a limited amount of Li doping, before the two-phase reaction is observed.

In the CuO system, the voltage decreases gradually until $Li = 0.3$ and then a plateau is seen at 1.35 V. The specific capacity is 600 mAh/g for discharge, which is 90% of the theoretical capacity (674 mA h/g). However, only 1/3 of this capacity (200 mA h/g) was obtained on charge.

3.3. Structural Investigation of Discharge and Charge Reaction Processes. *3.3.1. CuF_2.* 3.3.1.1. High-Resolution XRD. To investigate the phase transitions that accompany to electrochemical process, high-resolution X-ray diffraction was performed on the discharged CCN-CuF_2 materials stopped at different states of discharge (Figure 3). In the sample Li0.5 (i.e., the sample that contains 0.5 Li ions per CuF_2 formula unit), the main reflections from CuF_2 are still present, but now reflections from Cu metal are also clearly observed. Reflections from LiF are not clearly visible, which may be due to the small LiF particle sizes and their low concentration. In the Li1.0 sample, the reflections from Cu metal and LiF start to become more pronounced. At this point, very little CuF_2 appears to be present in the sample; the loss of CuF_2 reflections may also arise from a reduction in CuF_2 particle size during discharge (due to both the conversion reaction involving the CuF_2 particles, and particle cracking, which may be associated with this process), which can broaden the peaks beyond detection. The three peaks marked with asterisks are from Cu_2O, which most likely

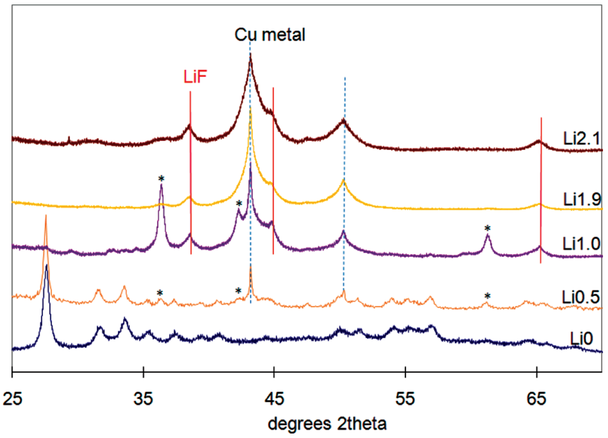

Figure 3. XRD patterns of the discharged CCN_CuF$_2$ samples. The reflections from LiF and Cu metal are marked with solid lines and dashed lines, respectively. The peaks marked with asterisks are from Cu$_2$O.

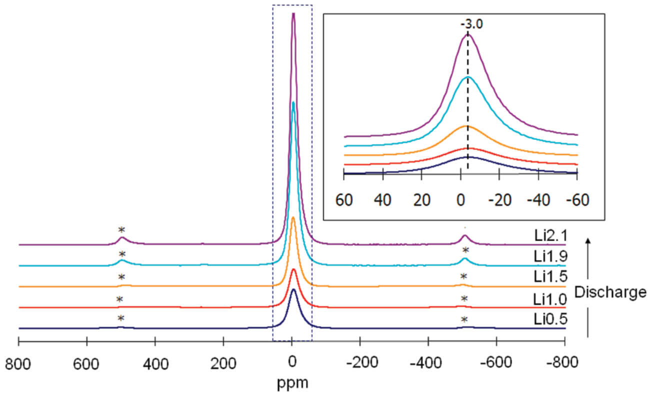

Figure 4. ^{7}Li MAS NMR spectra of discharged CCN-CuF$_2$ between Li = 0.5 and 2.1, acquired at a field strength of 4.7 T. The isotropic resonances and spinning sidebands are marked with their isotropic shifts and asterisks, respectively, in this and subsequent NMR spectra. The inset shows an enlargement of the isotropic resonances. The spectra were normalized on the basis of the number of acquisitions and mass of the samples.

result from the contamination of the sample by oxygen when it was kept in the Kapton capillary for the XRD measurements. The ready oxidation of the sample at this point may be due to the small particle sizes and the exposed surfaces area caused by cracking of the CuF$_2$ particles. At the end of discharge, only the reflections from Cu metal and LiF can be observed.

3.3.1.2. MAS NMR. The local structural changes that occur during the discharge process of CCN-CuF$_2$ samples were then investigated by using ^{7}Li, ^{19}F, and ^{63}Cu NMR spectroscopy. Only one ^{7}Li isotropic resonance is observed at −3.0 ppm in the ^{7}Li NMR spectra of the discharged CCN-CuF$_2$ samples, between Li=0.5 and 2.1, whose peak intensity increases gradually with state of discharge (Figure 4). This small chemical shift is a signature of a diamagnetic material and the resonance is assigned to the formation of LiF and salts in the SEI layer.[25]

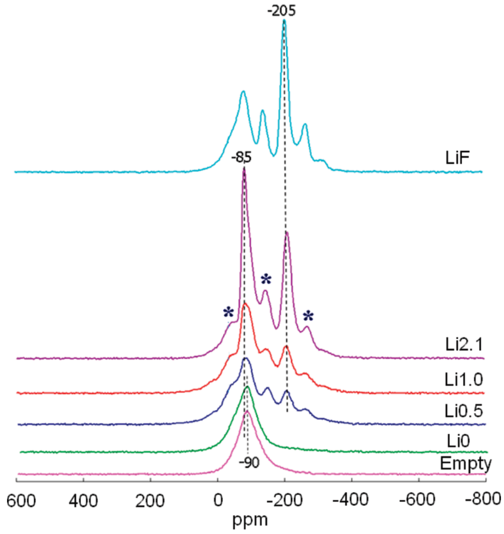

Figure 5. Normalized ^{19}F MAS NMR spectra (acquired at a field strength of 8.5 T) of discharged CCN-CuF$_2$ between Li = 0.5 and Li = 2.1. For comparison, the spectra of an empty rotor and LiF are shown.

^{19}F NMR was performed in order to distinguish between LiF and fluorinated components in the SEI layer (Figure 5). Because Cu^{2+} is paramagnetic and F is directly bound to Cu, the ^{19}F signal of CuF$_2$ cannot be readily observed, and thus the isotropic resonance at −90 ppm seen in the spectrum of pristine CCN-CuF$_2$ (Li0) is due to the fluorine background in the probe and the PVDF (−90 ppm) in the binder. Two more isotropic resonances at around −205 and −85 ppm appear in the Li0.5 sample, in addition to the −90 ppm peak, which are assigned to LiF and the SEI components (e.g., LiP$_x$O$_y$F$_z$),[26] respectively. The intensity of these two peaks increases with state of discharge. This indicates that LiF is formed right at the beginning of discharge, although no distinctive reflections due to LiF were seen in the XRD pattern of the Li0.5 sample (Figure 3).

In the spectra of the sample Li2.1, the peak at −85 ppm is much more pronounced than that in the sample Li1.0, which appears to indicate that the SEI formation is significant at the end of discharge. The signals from PVDF binder (present in all these samples) (−90 ppm) and LiPF$_6$ (−70 ppm) overlap with the background signal, and are not clearly resolved. In principle, the intensity due to PVDF should be a constant for each spectrum of an electrode material. It is possible that the PVDF in close proximity to the paramagnetic CuF$_2$ phase in the Li0.0 sample may be washed out, and that some of the −85 ppm signal in the Li2.1 phase (where the CuF$_2$ is absent) is actually due to PVDF. However, a similarly large signal at a similar shift position was observed following electrochemical insertion of Li in FeF$_3$, in electrode composites that do not contain PVDF,[27] suggesting that this signal is due to the SEI.

^{63}Cu NMR was performed to study the local environment of Cu and formation of Cu metal during the electrochemical process. ^{63}Cu has a natural abundance of

---

(25) Meyer, B. M.; Leifer, N.; Sakamoto, S.; Greenbaum, S. G.; Grey, C. P. *Electrochem. Solid-State Lett*. **2005**, *8*(3), A145–A148.

(26) Plakhotnyk, A. V.; Ernst, L.; Schmutzler, R. *J. Fluorine Chem*. **2005**, *126*(1), 27–31.

(27) Yamakawa, N.; Jiang, M.; Key, B.; Grey, C. P. *J. Am. Chem. Soc.*, in press.

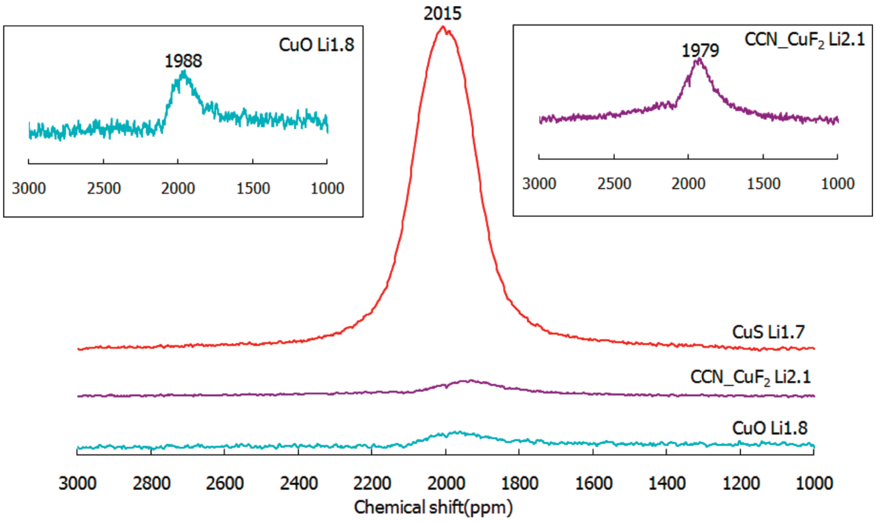

Figure 6. Static ^{63}Cu MAS NMR spectra of fully discharged CuS, CuF_2 and CuO for samples obtained with a silver NMR coil (at 4.7 T). The enlargements show the spectra for discharged CuF_2 and CuO.

69.09%, a spin I of 3/2, and a large quadrupole moment. The ^{63}Cu NMR spectra of samples Li1.0 and Li2.1 are dominated by an isotropic resonance at 2000 ppm, which is due to the Cu radio frequency (r.f.) coil in the probe (see the Supporting Information, Figure S1). No other signals are observed. However, according to the XRD data, Cu metal is present even in the early discharged samples. The loss of the signal due to Cu metal generated during discharge is ascribed to the small Cu particle sizes, the large electric field gradients present in these nanoparticles presumably resulting in very large quadrupolar interactions, broadening the signal beyond detection. Although Cu metal adopts a face-centered cubic structure with copper atoms sitting on cubic sites with no electric field gradients (and hence no quadrupolar coupling), most of the Cu atoms in nanoparticles are either at, or very near to the surface, and will sit in either lower coordinate sites or distorted local environments. Because the quadrupole moment of ^{63}Cu is so large, even small distortions from cubic symmetry will result in significant quadrupolar interactions, and the signals become extremely broad and difficult to detect. Static ^{63}Cu NMR was also performed with a probe with a purposely built silver coil, in order to detect weaker Cu signals, as shown in Figure 6. The probe contains a much smaller Cu background signal, which could be readily subtracted from the spectra of the samples. A very weak peak is now observed at 1979 ppm in the spectrum of the fully discharged CCN-CuF_2, presumably arising from Cu atoms in the center of larger nanoparticles, most likely the particles that give rise to the sharper reflections in the XRD patterns. In comparison to the signal observed for CuS on discharging (see below), the Cu metal signal in this compound is still very small. Interestingly, a slight decrease in the shift of this resonance is seen, in comparison to that of the bulk metal. Shifts in this system are dominated by the Knight shift, which is a measure of the density of states at the Fermi Level, and the small changes may reflect very slight changes in bonding in the Cu nanoparticles.

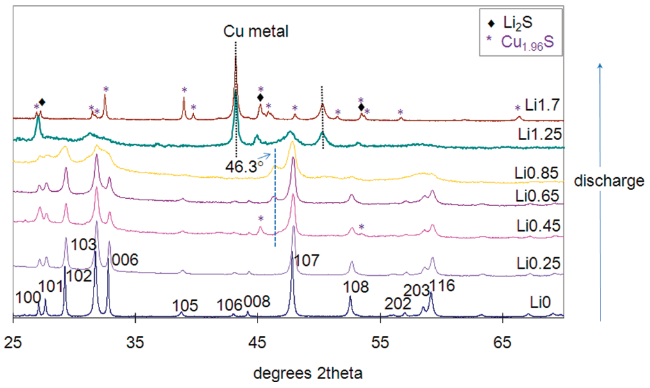

Figure 7. XRD patterns of the discharged CuS samples. The peaks from Cu metal are indicated with dashed lines, whereas those from Li_2S and $Cu_{1.96}S$ are labeled with ♦ and *, respectively. The sample Li1.25 was measured at X16C at the NSLS, and all the other samples were measured at 11-BM beamline at the APS.

3.3.2. CuS. 3.3.2.1. High-Resolution XRD. Figure 7 shows the XRD patterns of the CuS samples as a function of state of discharge. The pattern of the pristine CuS compound (Li0) shows that it is phase pure, and all the reflections can be assigned to a $P6_3/mmc$ space group. From Li0.25 to Li0.85, i.e., during the first process on the electrochemical curve, all the XRD patterns of these samples appear at first glance to be similar to that of the pristine compound. However, more careful examination reveals a few changes: For example, as shown in Figure 8a, although the CuS (002) peak at 10.7° 2θ stays at the same position in all the samples from Li0 to Li0.85, it broadens noticeably on lithiation, its intensity getting smaller with higher Li content and disappearing in the Li0.85 sample. An additional peak near 46.3°, which is not observed in the pristine compound, starts to appear in the Li0.45 sample and becomes more intense and well-resolved from the (107) peak in the Li0.85 sample. Figure 8b clearly shows that the reflections remain in the same position in all the discharged samples, but they are shifted noticeably in comparison to the reflections

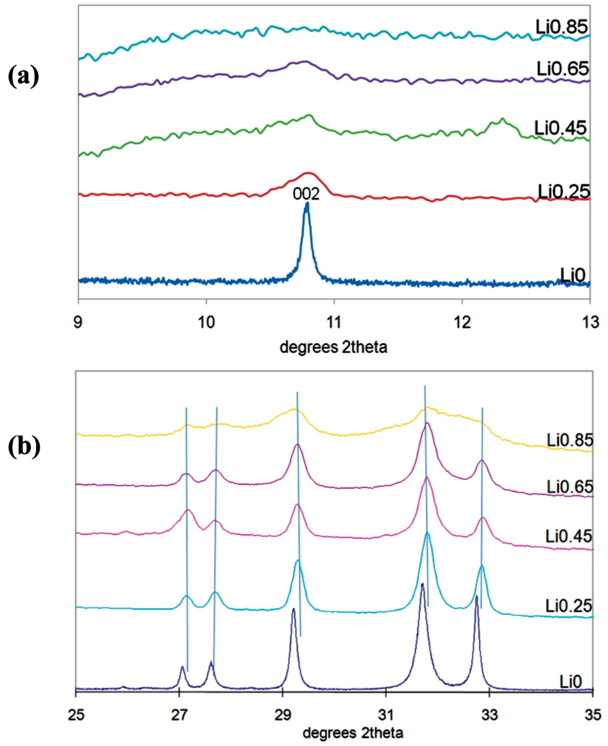

Figure 8. An enlargement of the XRD patterns for discharged CuS for Li = 0 to 0.85 (the first process) between (a) 9 and 13° 2θ and (b) 25 and 35° 2θ.

from pristine CuS. All the shifted peaks and the new reflection at 46.3° are assigned to a new phase, which appears to be structurally related to the CuS phase. This suggests that the insertion reaction on the first "plateau" is not a simple single-phase reaction as proposed previously, but it involves the formation of a new phase(s), via a two-phase reaction, consistent with the flat potential seen in the GITT measurement (Figure 2d) in the first half of the discharge process. Both the rapid broadening of the 002 reflection from Li0 to Li0.25 and the sloping potential seen by GITT at the onset of the lithiation suggest that CuS may tolerate some lithiation, before the onset of the two-phase reaction to form the new phase. No reflections from Cu metal and Li_2S are observed until Li = 0.85. Noticeable peak broadening is seen in the Li0.85 sample, which appears to indicate the onset of conversion reactions and particle cracking. The sample Li1.25 is in the middle of the second plateau, and its XRD pattern shows a mixture of several different phases. Reflection from Cu metal and Li_2S are clearly observed. The peaks at 30° and 47°, 2θ are reflections from the Li0.85 phase. At the end of the discharge, Li1.7, the XRD pattern is complicated and in addition to the peaks from Cu metal and Li_2S, a series of reflections from $Cu_{1.96}S$ are also observed.

Figure 9 shows the XRD patterns of the charged CuS samples. Once Li is extracted from the Li1.7 sample (i.e., the fully discharged state), very different XRD patterns are observed. The reflections from Cu and Li_2S are no longer obvious in the pattern of C_Li1.25, and all the reflections are at similar positions to those seen in the other two charged samples C_Li0.8 and C_Li0.35, (i.e., a lithiated CuS phase has reformed), except for the reflection at around 32° 2θ, which appears to correspond to a reflection from a phase related to $Cu_{1.96}S$ that is still present in the C_Li1.25 sample. Interestingly, the patterns are closer to that of the discharged sample Li0.85 than that of the pristine CuS (sample Li0), although many of the peaks in these patterns can also be observed in the reflections of the pristine CuS sample.

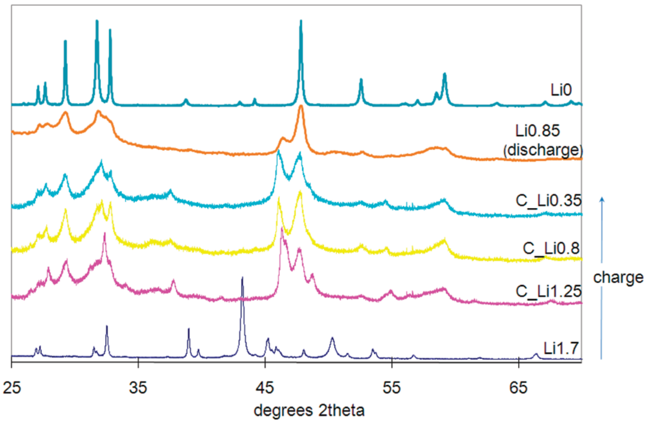

Figure 9. XRD patterns of the charged CuS samples. The patterns compared are those from pristine CuS and the discharged sample, Li0.85.

3.3.2.2. MAS-NMR. Two resonances are observed in the spectrum of the Li0.45 sample acquired at 8.5 T, one at −1 ppm, and the other, much weaker one, at −10 ppm (Figure 10). The peak at approximately −1 ppm is assigned to SEI layer and electrolyte salt, and possibly Li nearby Cu^{1+} ions in the intercalation phase Li_yCuS phase.[14] The peak at −10 ppm is assigned to Li ions nearby the remaining Cu^{2+} ions in the insertion phase Li_xCuS, the larger negative shift resulting from the unpaired electrons present on the paramagnetic ion Cu^{2+} ions. In the spectra of the sample Li0.85, the peak at −10 ppm is barely discernible, and a weak peak at 2 ppm due to Li_2S starts to appear. As more Li ions are inserted into the material, the 2 ppm Li_2S resonance becomes more and more pronounced, which is consistent with Li_2S formation during this region of the discharge curve.

During the charge process, from Li1.7 to C_Li0.45, the intensity of the Li_2S peak decreases gradually and only the peak from the SEI/Li_yCuS at −1.3 ppm is observed at the end of charge. The spectra were not acquired under conditions which allowed for a direct comparison of the peak intensity between samples, because the spectra were not acquired using identical spectrometer and probe conditions. Thus, to track the formation/loss of Li_2S, the ratio of the intensity of the Li_2S (2 ppm) resonance to Li_yCuS and SEI layer −1 ppm resonance is plotted in Figure 11 for each sample, the ratio increasing with state of discharge, decreasing with state of charge. The noticeable onset of significant Li_2S formation after Li = 0.8 (in the second region/plateau; 1.68 V) is now very clear, the Li_2S being reconverted on charge. Spectra were acquired at lower fields (4.7 T; see the Supporting Information, Figure S2) under conditions that did allow for a quantitative comparison of Li intensity. These did show a gradual increase in intensity as the discharge proceeds,

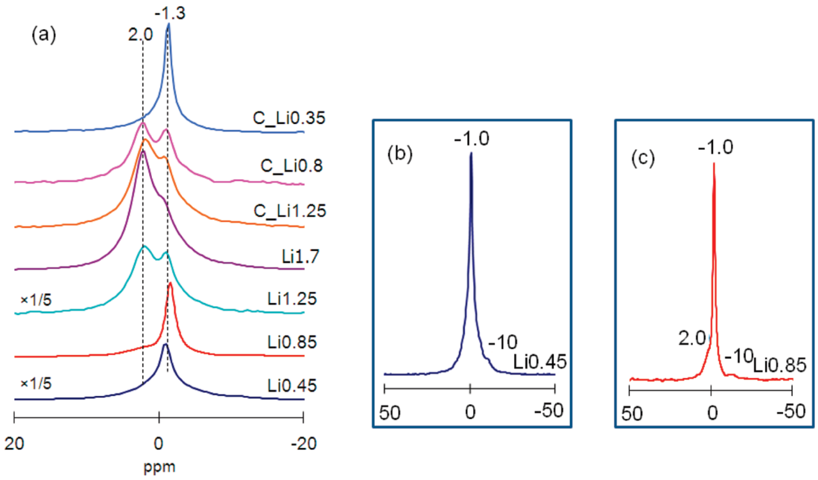

Figure 10. (a) ^{7}Li MAS NMR spectra of discharged CuS between Li = 0.5 and Li = 1.7 and charged CuS between Li = 1.7 and 0.35, acquired at a field strength of 8.5 T. (b, c) Spectra of the Li = 0.45 and 0.85 samples plotted over a larger frequency range.

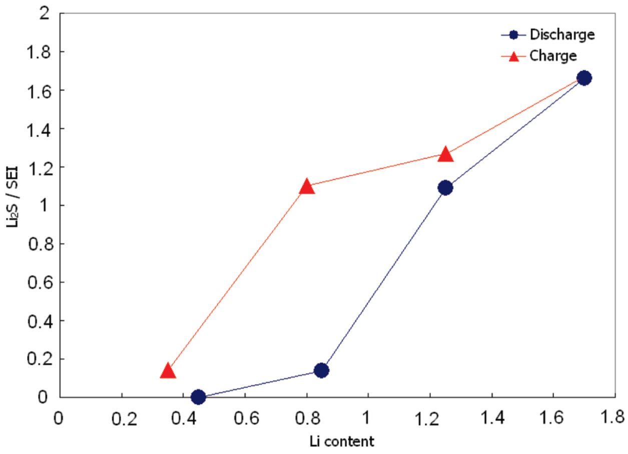

Figure 11. Li_2S/(SEI + Li_yCuS) ratio plotted as the function of Li content, during discharge and charge, for CuS.

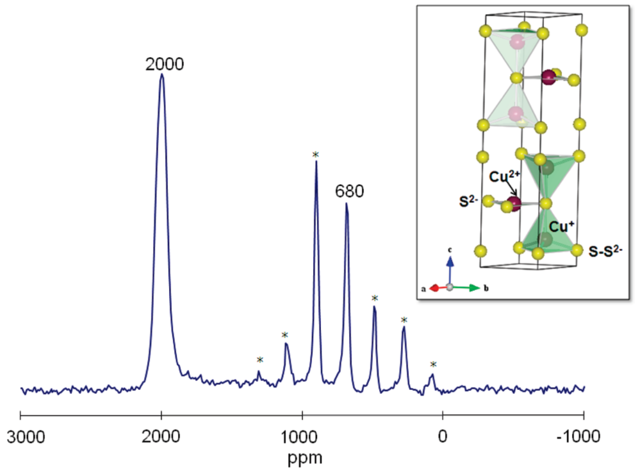

Figure 12. ^{63}Cu MAS NMR spectrum of pristine CuS acquired with a magnetic field strength of 4.7 T. The inset shows the crystal structure of CuS. The purple and yellow spheres correspond to Cu and S, respectively.

intensity decreasing gradually in intensity in discharge, tracking the Li content of the sample. Unfortunately only one isotropic resonance could be observed at this field strength, however, a noticeable shift of this resonance from −0.4 to −0.7 ppm for Li0.45 and Li0.85 to 0.5 and 1.18 ppm for Li1.25 and Li1.7, respectively, is consistent with the formation of Li_2S (2 ppm) formation in the later stages of the discharge.

Figure 12 shows ^{63}Cu NMR spectrum of pristine CuS, two resonances being observed at 2000 ppm and 680 ppm. The peak at 2000 ppm corresponds to Cu metal from the probe coil, as mentioned above, while the resonance at 680 ppm must correspond to CuS itself. This latter resonance is not due to a diamagnetic copper(I) compound Cu_2S ($Cu^{1+}{}_2S^{2-}$) impurity because we were not able to detect a resonance from this compound in the ^{63}Cu spectral region between −3000 and 7000 ppm in a separate experiment performed with an NMR rotor containing Cu_2S only. Cu_2S (chalcolite) contains Cu^{1+} ions in 3-coordinate in planar environments in an hcp array of S atoms, with four out of the 96 Cu^{1+} atoms in the unit cell possibly adopting a linear 2-fold coordination environment.[28] These low symmetry environments will be associated with very large ^{63}Cu quadrupolar coupling constants, the resulting second order quadrupolar interaction presumably broadening the resonance beyond the detection limit of these experiments.

To confirm the assignment of the 680 ppm resonance to CuS, a series of discharged CuS samples were examined (Figure 13). The intensity of the 680 ppm peak in the pristine CuS sample, Li0, is the highest, decreasing noticeably on adding only 0.3 Li. The intensity then drops steadily with more Li content in the sample and is totally invisible in the discharged sample Li0.85 as well as in the charged C_Li0.5 sample. As suggested previously,[29] CuS is a mixed valence compound containing both S^{2-} and $S-S^{2-}$ anions. Its formula is more accurately expressed as $Cu^{2+}S^{2-}(S-S)^{2-}Cu_2{}^{2+}$, where the Cu^{2+} ion is coordinated to three S^{2-} ions and the Cu^{+} ion is located in a tetrahedral site with three S^{-} ions and one S^{2-} ion, as

---

(28) Evans, H. T. *Science* **1979**, *203*(4378), 356–358.

(29) Pattrick, R. A. D.; Mosselmans, J. F. W.; Charnock, J. M.; England, K. E. R.; Helz, G. R.; Garner, C. D.; Vaughan, D. J. *Geochim. Cosmochim. Acta* **1997**, *61*(10), 2023–2036.

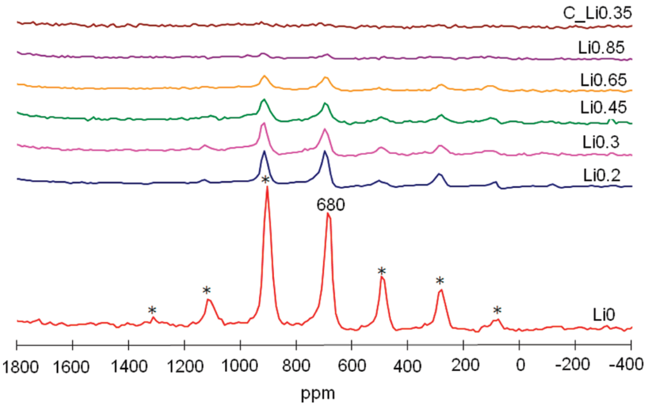

Figure 13. ^{63}Cu MAS NMR spectra of discharged CuS between Li = 0 and Li = 0.85 and charged CuS with Li = 0.35 in the region between −400 and 1800 ppm. This and the subsequent ^{63}Cu NMR data were acquired with a copper coil.

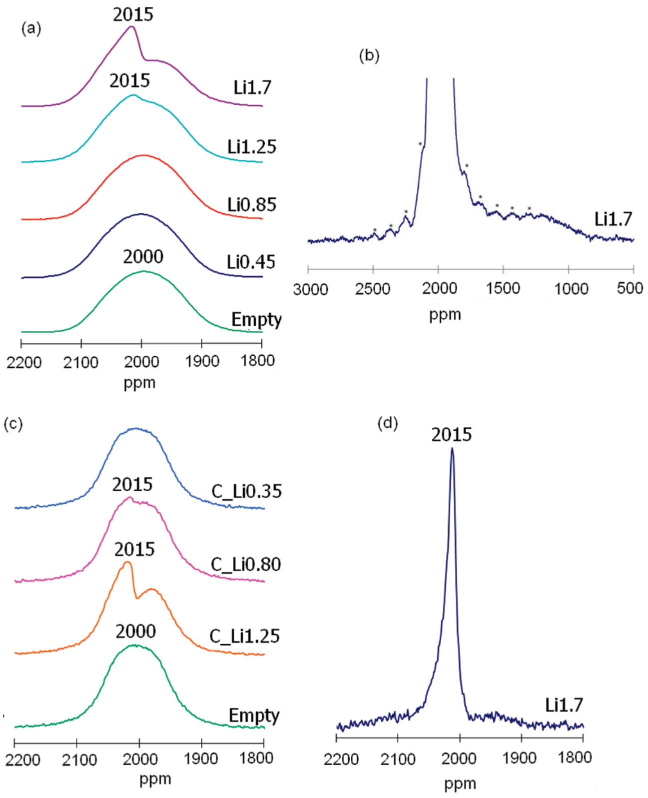

Figure 14. ^{63}Cu MAS NMR spectra of (a) discharged CuS between Li = 0.45 and Li=1.7 acquired in 4.7 T, and (b) the fully discharged sample, Li 1.7, acquired at 8.46 T. The isotropic resonances are truncated in this spectrum so as to show the spinning side bands from the peak at 2015 ppm. Spectra collected at 8.46 T from (c) CuS on charge, between Li = 0.35 and Li=1.7 ppm, and (d) the fully discharged sample Li 1.7.

shown in the inset in Figure 12. Because Cu^{2+} (d^9) is paramagnetic, the hyperfine shift of the Cu^{2+} ion will be extremely large and the Cu^{2+} ions cannot be observed in the frequency range of this experimental set up. Thus, the peak at 680 ppm is assigned to the Cu^{1+} ions in the tetrahedral site of the structure. The Cu^+ that forms on discharge in Li_xCuS or in LiCuS must be in too distorted an environment to be detected by NMR.

Figure 14a shows an enlargement of the ^{63}Cu spectra of the discharged CuS samples in the 2000 ppm region. Only the peak from Cu coil is observed in the Li0.45 to Li0.85 samples. However, in the spectra of the samples Li1.25 and Li1.7, which are on the second plateau in the discharge profile, an extra resonance at 2015 ppm is observed, which is well resolved from the peak of the Cu coil (at 2000 ppm). Spinning side bands from this resonance are observed (Figure 14b), confirming that this signal arises from a material in the NMR rotor and not from any probe background. The intensity of the 2015 ppm resonance is higher in the Li1.7, than that in Li1.25 sample, and hence this peak is assigned to the Cu metal formed during the discharge. This confirms that the conversion reaction that takes place mostly after Li=1.0 results in the formation of large Cu metal particles.

The static ^{63}Cu NMR spectrum of the fully discharged sample, acquired with the silver coil, confirms the formation of Cu metal at the end of discharge (Figure 6), and clearly demonstrates that the Cu particles are much larger and/or more ordered than those formed in the LiF/Cu nanocomposite, where the signal from Cu was very difficult to detect. The ^{63}Cu NMR spectra of the charged samples are shown in Figure 14c. Because these spectra were acquired at a higher field strength (8.5T), the ^{63}Cu spectrum of the fully discharged sample Li1.7 (Figure 14d) also acquired at 8.5 T is shown for comparison. The ^{63}Cu signals are much more intense at this higher magnetic field strength (Figure 14a) and the background signal from the Cu coil is reduced noticeably. This is presumably a consequence of the greater sensitivity of the higher field experiments, the different probes used in the experiments, and possibly the reduction of any second-order quadrupolar effects for Cu environments with nonzero electric field gradients. The Cu metal peak decreases in intensity dramatically in the samples C_Li1.25 and C_Li0.80 compared to the signal of the fully discharged sample Li1.7 and it disappears completely in the sample C_Li0.45. Note however, that Cu metal is still seen at intermediate states of charge, even though the reflections from Cu are absent from the XRD patterns.

3.3.3. CuO: XRD and MAS NMR. XRD diffraction of the fully discharged sample Li1.8 was performed (Figure 15), and it shows that CuO has reacted to form very small Cu particles (approximately 2.7 nm). Reflections due to Li_2O are barely discernible above the noise, which is ascribed to the small particle size of this phase, and the weak scattering of Li and O, in comparison to copper. The ^{7}Li NMR spectra were acquired for a larger subset of the discharged CuO samples (Figure 16). The spectrum of sample Li0.1 and Li0.3 contains a single broad resonance at approximately −3.6 to −4.2 ppm, the resonance shifting to higher frequencies and increasing in intensity on further lithiation. The line shape is asymmetric, which suggests that more than one peak contributes to this resonance.

The shift to higher frequencies at higher lithiation levels is ascribed to the presence of Li_2O, which resonates at 2.8 ppm. Two resonances could be resolved in the spectrum of the Li1.8 sample, acquired at a higher field

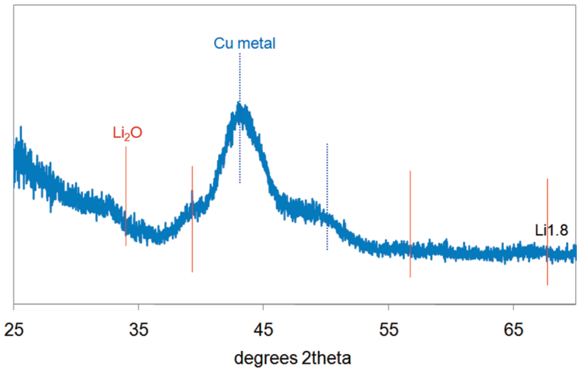

Figure 15. XRD pattern of discharged CuO sample Li1.8. The positions of the reflections from Cu metal and Li_2O are indicated with blue dashed and red solid lines, respectively.

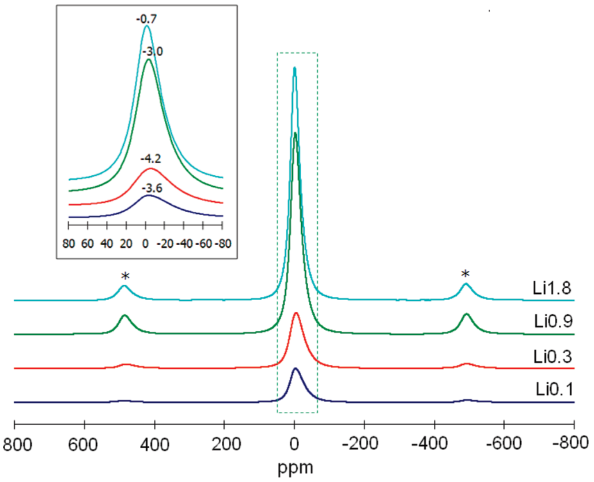

Figure 16. ^7Li MAS NMR spectra of discharged CuO between Li = 0.1 and Li = 1.8. The inset shows the isotropic resonances.

strength of 8.46 T, at 2.8 and 1.0 ppm, consistent with this suggestion. The resonance at 1.0 is ascribed to the SEI. The resonances at -3.6 to -4.2 ppm at low lithation levels must contain a large contribution from (overlapping) resonances with more negative shifts. This suggests that an insertion phase such as Li_xCuO may be formed during discharge, giving rise to Li^+ ions nearby Cu^{2+} ions, with presumably resonances with negative frequencies. Novak et al.[19] have already proposed the electrochemical insertion of the lithium into CuO structure according to the following reaction:

$$CuO + xLi \rightarrow Li_xCuO \quad (0 < x < 1) \tag{7}$$

which appears to be in agreement with our NMR results, but further NMR experiments with more samples at higher fields are required to confirm this hypothesis.

The ^{63}Cu NMR spectra of the discharged CuO sample Li1.8 (at the end of discharge), obtained with the NMR probe containing the copper coil, is essentially identical to that of the empty rotor seen in Figure S2 in the Supporting Information and Figures 3 and 14. Only one isotropic resonance corresponding to the Cu coil is observed, and no change in the intensity is observed between the spectra of the discharged sample and the empty rotor. No signal is seen at 0 ppm, indicating that Cu_2O is not formed. The loss of the signal from the Cu metal is ascribed to the same cause as in the CuF_2 system, i.e., the small particle sizes formed on discharge. A very weak peak at 1988 ppm can, however, be observed in the static ^{63}Cu NMR spectrum of the fully discharged sample (Figure 6) obtained in the probe containing the silver coil, which is assigned to Cu atoms in the center of the nanoparticles and/or in larger nanoparticles.

4. Discussion

4.1. Discharge Reaction Mechanisms in the CuF_2 System. The discharge reaction of CuF_2 is relatively straightforward. Cu is formed right from the beginning of discharge as seen by XRD. Although the reflections from LiF are not very pronounced at the early stage of discharge, which may be due to the small LiF particle sizes, the ^{19}F NMR signal of LiF can be clearly observed in the discharged Li0.5 sample. The reduction of Cu^{2+} to Cu^+ is unlikely to be occurring in this compound, because a higher operating voltage than observed experimentally is predicted for this redox couple.[10] This is in agreement with the ^7Li NMR results because no resonances are observed from any potential insertion compounds. Only an isotropic resonance at -3 ppm is seen, which is assigned to LiF and Li salts in the SEI layer. On the basis of this data, a simple conversion reaction is taking place from the beginning of the discharge process, and the reaction mechanism of CuF_2 can be written as follows

$$CuF_2 + 2Li^+ + 2e^- \rightarrow Cu + 2LiF \tag{8}$$

The discharge curve is however divided into two regions: a "plateaulike" region from Li0 to Li1.0 that is associated with the conversion reaction described in eq 8, and a sloping voltage region from Li1.0 to Li2.1. The sloping voltage does not appear to reflect a different process, but must arise from differences in the kinetics of the process and/or the electronic/ionic conductivity of the nanocomposite. As shown in the XRD patterns (Figure 3), the reflections from Cu metal in the Li0.5 sample are sharp, indicating that the first few particles of copper that are formed are larger (approximately 60 nm, based on the Scherrer formula), but as the reflections grow in intensity, they broaden, indicating that progressively smaller Cu particles or domains are formed as the reaction proceeds. In the fully discharged sample Li2.1, the reflections of Cu metal are a combination of a weak sharper component and a much larger broader component. This is consistent with the ^{63}Cu NMR signal, where only a weak signal from the larger Cu metal particles was observed.

Interestingly, the copper metal that first forms has a larger X-ray coherence length than the CuF_2 particles themselves (~60 vs 16 nm), suggesting that some of the peak broadening seen in the XRD patterns of the pristine CCN-CuF_2 particles arises from the disorder introduced by the ball-milling and not just the decrease in particle size. Finally, based on the strong resonance at -85 ppm seen in the fully discharged sample (Li2.1), the extent of SEI formation appears to be significant. Further experiments are now in progress to explore this in more detail and to examine the extent to the SEI formation is reversible.

4.2. Discharge and Charge Reaction Mechanism in CuS System. The discharge process of CuS can be divided into two steps according to the electrochemical profile. From Li0 to Li0.85, i.e., during the first process, no evidence for any significant Cu metal and $\mathrm{Li_2S}$ formation is observed in both the ^{63}Cu and ^{7}Li NMR spectra and the XRD patterns. However, a noticeable change in observed between the Li0.0 and Li0.25 XRD patterns and then on subsequent lithiation. The (002) reflection from the CuS phase at 10.7° 2θ broadens almost immediately and then gradually disappears, while a peak from a new phase at 46° 2θ appears during this region of the discharge process. In addition, a weak resonance at -10 ppm is observed in the ^{7}Li NMR spectra, which is assigned to $\mathrm{Li^+}$ nearby $\mathrm{Cu^{2+}}$ in an intercalation phase $\mathrm{Li}_x\mathrm{CuS}$, along with a strong resonance at approximately -1.0 ppm due to a combination of the SEI and $\mathrm{Li^+}$ ions nearby $\mathrm{Cu^{1+}}$ in the intercalation phase, $\mathrm{Li}_y\mathrm{CuS}$ ($y > x$).

The X-ray coherence length of the CuS particles, as determined by the (002) reflections decreases significantly between $\mathrm{Li} = 0$ and 0.25, whereas the coherence length derived from the reflections at larger values of 2θ remains essentially unchanged. Thus, it appears that CuS can accommodate a small amount of Li (less than 0.16, based on the GITT experiment), without significant change of structure. Insertion of $\mathrm{Li^+}$ can occur via the reduction of the $\mathrm{Cu^{2+}}$ ions located in the trigonal sites (Figure 12), and the $\mathrm{Li^+}$ can be readily accommodated if the $\mathrm{Cu^{2+}}$ ions move off these sites into either the vacant octahedral or tetrahedral sites above and below the trigonal sites, leaving tetrahedral/octahedral sites free for the $\mathrm{Li^+}$. This movement of the Cu ions may be responsible for the loss of intensity of the (002) reflection. The subsequent flat voltage profile, along with the lack of change in position and intensity of the main CuS reflections, from $\mathrm{Li}=0.25-0.65$, combined with the gradual growth of a new reflection at 46° 2θ, is consistent with the formation of a new but structurally related intercalation phase $\mathrm{Li}_y\mathrm{CuS}$, where $y \geq 0.90$ (based on the GITT experiments). Insertion of up to 0.5 $\mathrm{Li^+}$ ions can occur via the reduction of the $\mathrm{Cu^{2+}}$ ions but further reduction must proceed via the reduction of the $\mathrm{S{-}S^{2-}}$ ions, possibly associated with $\mathrm{Li^+}$ insertion between the sulfur layers. It is clear that the processes that occur in this range are complex, and more structural studies are required to understand in more detail the nature of the structural transformations. However, based on a combination of the electrochemistry and diffraction results, we propose the following sequence of events

$$x\mathrm{Li} + \mathrm{CuS} \rightarrow \mathrm{Li}_x\mathrm{CuS} \quad (0 < x \leq 0.16) \tag{9}$$

$$\mathrm{Li}_x\mathrm{CuS} + (y-x)\mathrm{Li} \rightarrow \mathrm{Li}_y\mathrm{CuS} \quad (y \approx 1) \tag{10}$$

This mechanism is consistent with Chung et al.'s results,[14] but differs from that of Debart et al.,[15] who proposed that $\mathrm{Cu_2S}$ and $\mathrm{Li_2S}$ are formed in the first step. However, the intensity of the ^{7}Li NMR resonance from $\mathrm{Li_2S}$ (Figure 10) is too weak for the samples with $\mathrm{Li} < 1.25$ to be consistent with a major process involving $\mathrm{Cu_2S}$ (and $\mathrm{Li_2S}$) formation. The formation of $\mathrm{Cu_2S}$ from CuS involves migration of $\mathrm{Cu^{1+}}$ from the surface into the CuS phase, while the formation of $\mathrm{Li}_x\mathrm{CuS}$ only requires the migration of $\mathrm{Li^+}$. Because both ions are mobile, it is possible that both mechanisms occur to some degree in the first plateau, accounting for the observation of some $\mathrm{Cu_{1.96}S}$ in the high-resolution TEM studies of this group;[15] it is also possible that this phase results from the decomposition of $\mathrm{Li}_x\mathrm{CuS}$ under the electron beam.

At Li0.85, $\mathrm{Li_2S}$ starts to be formed in significant quantities and the reflections of the $\mathrm{Li}_y\mathrm{CuS}$ phase broaden very rapidly as the second process commences. The broadening of reflections, which actually starts between $\mathrm{Li}=0.65-0.85$, indicates either a decrease in the domain size of the intercalation phase and/or increased disorder. On the basis of the GITT curve, it is clear that some Cu extrusion is now competing with the intercalation process, presumably causing the particle cracking/reduction in domain size. Cu is extruded from the phase in form of large Cu particles (38 nm), which are clearly seen by both XRD and NMR. A series of reflections from $\mathrm{Cu_{1.96}S}$ are also observed in the XRD pattern of fully discharged sample Li2.0, in addition to the reflections from Cu and $\mathrm{Li_2S}$. The appearance of $\mathrm{Cu_{1.96}S}$ is largely ascribed to the decomposition product of the unstable $\mathrm{Li}_y\mathrm{CuS}$ phase. This is different from that proposed by Chung et al.,[14] who suggested that $\mathrm{Cu_{1.96}S}$ was formed via an electrochemical process. However, the reflections from $\mathrm{Cu_{1.96}S}$ are not observed in all the discharged samples and there is no systematic trend associated with the appearance/disappearance of this phase. Because a capacity of only 477 mA h/g corresponds to a 1.7 Li discharge capacity, this suggests that not all of the $\mathrm{Li}_y\mathrm{CuS}$ is converted to Cu metal and $\mathrm{Li_2S}$. We propose that at least some of the missing capacity arises from the fraction of the phase that is involved in the decomposition reaction. The second process can, therefore, be described as follows

$$(1-z)(\mathrm{Li}_y\mathrm{CuS} + \mathrm{Li^+} + e^- \rightarrow \frac{1+y}{2}\mathrm{Li_2S} + \mathrm{Cu}) \quad (y \approx 1) \tag{11}$$

At the same time, the disproportionation reaction can occur:

$$z(\mathrm{Li}_y\mathrm{CuS} \rightarrow 0.5\mathrm{Cu_{1.96}S} + 0.02\mathrm{Cu} + \frac{y}{2}\mathrm{Li_2S}) \tag{12}$$

On the basis of the loss in capacity and assuming that the $\mathrm{Cu_{1.96}S}$ is not reduced further, $z \approx 0.3$, at least in our cells, based on the discharge capacity of 477 mA h/g. Furthermore, we suggest that this reaction accounts for some loss in capacity during the first process, making it difficult to determine the exact composition of the insertion phase $\mathrm{Li}_y\mathrm{CuS}$, and resulting in the formation of a weak $\mathrm{Li_2S}$ resonance even before a significant concentration of Cu metal is observed. The factors that control the extent of

$Cu_{1.96}S$ formation are not, however, clear at this point and are presumably influenced by parameters such as the discharge and charge rates and how long the samples were allowed to rest before the XRD/NMR measurements.

During charge, the conversion reaction is reversed, with both the XRD and Cu NMR results showing the disappearance of Li_2S and Cu metal. The XRD patterns are quite similar for all the charged samples, and resemble those of the intercalation phase seen on discharge. It appears that the charge process follows a similar route to the discharge process and that a $Li_{y'}CuS$-like phase (or phases) forms during charge. The reaction on charge can be written as follows (assuming $z \approx 0.3$):

$$0.85Li_2S + 0.76Cu + 0.15Cu_{1.96} \rightarrow Li_{y'}CuS \rightarrow Li_{0.35}CuS + 1.35Li \qquad (13)$$

where the Li content is calculated on the basis of the charge capacity obtained electrochemically. On the basis of the XRD, however, it is likely that the intercalation phases that form on charge may differ slightly in terms of their different local and long-range arrangements of the Cu, Li, and S ions. Further structural studies are required to investigate this.

4.3. Comparison of the Conversion Processes. The sizes of the particles formed during the conversion reactions are different for the three systems and vary as a function of state of discharge and any mechanism proposed for systems must take these observations into account. For example, the particle sizes of the Cu metal formed during the discharge, as derived from the XRD patterns are very different for the Cu produced from CuO, CuF_2, and CuS (3, 9, vs 38 nm, respectively, at the end of discharge). However, the Cu that first forms in the fluoride system has noticeably larger particle sizes than the Cu formed at the end of the discharge (60 vs 9 nm). However, this phenomenon is not seen for the CuS system. The formation of composites with smaller metal/LiX domains is often thought to help in the electrochemical reversibility on charge, however, the reversibility of CuS is much better than that of CuF_2 and CuO. Clearly, some of the factors that are responsible for the formation of the larger particles, such as high Cu mobility and electronic conductivity, will also favor the reversible reaction.

The nucleation and growth of the different phases that form during the conversion reactions, and thus the morphologies and sizes of the particles within the nanocomposites, are governed by a number of factors which include the (i) relative rates of diffusion of the cations, anions and Cu atoms/ions through the original starting material, intermediate (intercalation) phases, the final salts (LiF and Li_2X (X = O, S)), and at the grain boundaries/interfaces between these phases, and (ii) the electronic conductivities of the different components.[8] Considering the effect of cation diffusion first, Cu^{1+}-ion diffusion is generally much faster than Cu^{2+}-ion diffusion due to the lower charge of the ion, and cation diffusion in the copper sulfides will be enhanced over diffusion in the oxides and fluorides, due to the larger polarizability of the sulfide ion. Rapid mobility of the $Cu^{1+/2+}$ ions will tend to favor growth over nucleation, because the ions, particularly in the Li_yCuS phases, can migrate to the CuS/Cu interfaces allowing the Cu particles to grow. Migration of Cu^0 atoms at the interfaces will also help in particle sintering. Li^+ ion diffusion can occur, in principle, in the original phase, any intercalation compound, and in LiF/Li_2X, the conductivity in the final salts decreasing in the order $Li_2S > Li_2O \gg LiF$, due to both structural factors and the decrease of the polarizability of the anion. O^{2-}, and particularly S^{2-} mobility are generally much lower than Li^+ and Cu^{1+} mobility due to their large sizes and charge (for O^{2-} and S^{2-} [13]), but fluoride diffusion may play an important role in the CuF_2 phase. Ionic conductivity of both ions in LiF is, however, expected to be poor because of its structure type (rocksalt). Finally, the third factor to be considered is the electronic conductivity of the original phases, the intercalation compounds and of the nanocomposites. Increased electronic conductivity of the particles allows the reduction of the Cu^{2+}/Cu^+ via reaction with Li^+ (and transport of the electron through the CuX/CuF_2 phase) to occur on all the surfaces/internal interfaces of the CuX/CuF_2 particles, instead of it being limited to sites nearby the carbon/$CuX(CuF_2)$ interfaces, without resulting in a large overpotential. The interplay between all these factors will lead to complex mechanisms that control reactivity, particle sizes and morphologies. We now propose a series of mechanisms that are likely to be important in these classes of materials.

The CuF_2 system is the simplest to consider first because this phase is a poor electronic conductor, which does not form an intercalation phase. LiF is formed, which is both poor ionic and electronic conductor; however, F^- conduction in CuF_2 will occur, to some extent. Presumably, the first CuF_2 particles to be reduced are those in direct or close contact to the carbon particles, because of the poor electronic conductivity of CuF_2. Copper is extruded from the particles and nanoparticles of LiF are formed. Between Li = 0 and 0.5, larger Cu particles are seen by XRD; no LiF is observed by XRD, but it is seen by NMR, indicating that its particle size is small. We ascribe these observations to relatively rapid fluoride ion transport away from the CuF_2/Cu metal interface to the CuF_2/electrolyte interface, where it can react with more Li^+ to form LiF. Copper metal is then left near the carbon current collector, initially forming relatively large particles. This is illustrated in the cartoon shown in Figure 17. As the reaction progress, the fluoride ions will have to migrate further from the carbon, either through the CuF_2 phase, or along the $Cu-CuF_2$ interfaces, so as to reach a surface uncoated with LiF. However, this F^- transport should compete favorably with Li^+ and F^- migration through the LiF coatings that form on the surface, because of the poor ionic conductivity of LiF. If cracks form in the LiF, some reaction may also involve Li^+ migration through the CuF_2/Cu interfaces (grain boundaries)[8] forming an insulating LiF coating at this interface, as shown schematically in Figure 17b. As

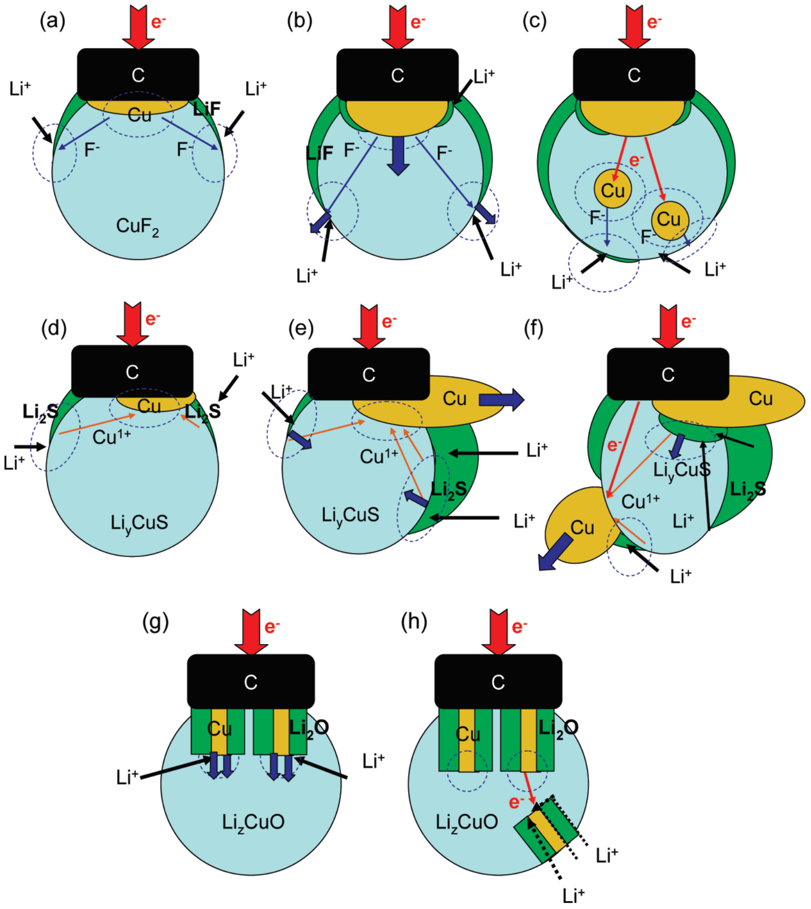

Figure 17. Schematics illustrating possible reaction pathways for the three systems, assuming a single electrical contact to a Li_zCuX_n particle. (a−c) CuF_2, (d−f), CuS, and (g, h) CuO. In all the figures, the interface and growth direction of the interface are indicated by dashed blue circles and blue arrows respectively. For CuF_2, transport of F^- (blue arrows) from the Cu/CuF_2 interface to the CuF_2/LiF/electrolyte interface is important (a, b). As the reaction progresses, electron tunneling (red arrows), may result in the formation of Cu nuclei not directly located on the Cu/carbon interface (c). In CuS, Cu^{1+} diffusion (brown arrows), away from the LiCuS/Li_2S interface to the LiCuS/Cu interface occurs (d, e), Li^+ diffusion (black arrows) to the LiCuS/Li_2S interface occurring both through the Li_2S and directly from Li^+ the electrolyte. Better electronic conductivity of this phase (over CuF_2) allows Cu nuclei to form away from the carbon current collector (f). In CuO (and CuF_2, at least to some degree), a mechanism involving a triple phase boundary is expected to dominate, involving Li^+ diffusion through the slightly lithiated phase, Li_xCuO, to the moving boundary, the boundary initially grows away from the carbon current collector (g), but later on, in different parts of the particle (h).

this reaction proceeds, the resistance associated with the increasingly longer range fluoride migration/transport through CuF_2 and Cu/CuF_2 interfaces (and to a degree, LiF) will increase, and the overpotential of the reaction will increase. A striking experimental observation is the correlation between the loss in the CuF_2 reflections and the rapid decrease in the overpotential of the reaction at approximately $Li = 1.0$. We propose that at around this point, some Cu starts to nucleate within the larger CuF_2 particles, breaking the particles apart to form CuF_2/Cu nanodomains. This represents an “internal reduction mechanism”, where the product destroys the matrix lattice on reduction, a process that has been well-studied for metal oxides, for chemical reduction.[30] This mechanism will occur when cation mobility is slower than anion mobility, but it does require electronic conductivity. However, the overpotential has now increased sufficiently that electronic tunneling through the CuF_2 particle to more distant Cu^{2+} ions may become competitive with processes involving longer range fluoride-ion conduction to the surfaces of the LiF-coated CuF_2 particles. We note also that the CCN-CuF_2 nanocomposites will have multiple carbon-CuF_2 contacts, so that the electron tunneling distances will be small. Because the metal particle, in this case Cu^0, is associated with a different volume, this results in large stresses and strains[30] and particle cracking. Particle cracking may also reduce the difficulty associated with Li^+ diffusion, as it will create pathways for Li^+ to approach the reaction sites. The additional electronic conductivity of the nanocomposite due to the formation of copper nanoparticles does not appear to help reduce the overpotential significantly, consistent with the model where the formed Cu particles are surrounded initially with CuF_2, and then eventually with LiF toward the end of the reaction.

The reaction mechanisms for CuS are very different for three main reasons. First, the initial formation of intercalation compounds such as Li_xCuS ($0 < x \leq 0.16$) and Li_yCuS ($y \approx 1$) will enhance the Cu ionic conductivity, because more Cu^{1+} ions are formed, and the disorder in the system increases. Second, the higher electronic conductivity of these sulfide phases[13] will allow the

---

(30) Schmalzreid, H.; Backhaus-Ricoult, M. *Prog. Solid State Chem.* **1993**, *22*, 1–57.

Li_yCuS/Cu interface to occur anywhere in the particle, not just near the parts of the particle electronically connected (e.g., via the carbon) to the current collector. Third, more rapid Li^+ diffusion in Li_2S will also allow a thicker Li_2S film to form and, more importantly, diffusion of the Li^+ through the Li_2S to the Li_2S/Li_yCuS interface. As shown in illustrations d and e in Figure 17, this will result in Cu particles or dendrites that grow away from the Li_yCuS particles, the Li_2S phase growing into the Li_yCuS phase. This is opposite to what was proposed to occur for CuF_2 but is consistent with the large Cu dendrites seen by TEM by Debart et al. in the fully discharged product.[15] As illustrated in Figure 17f, Li^+ transport through Li_yCuS can also occur, which could cause the Li_2S interface to grow directly on the Cu particle. Eventually, this may prevent further growth of the Cu particle (by blocking the Cu^+ diffusion), encouraging growth of other Cu nuclei that form on Li_yCuS surface, or in the particle, the latter resulting in particle cracking. The transformations that occur in this system are further complicated by the decomposition of the unstable Li_yCuS phase to form $Cu_{1.96}S$ and Li_2S as described by reaction 10. This process is mediated by the diffusion of both the Cu^{1+} and Li^+ ions. It is not clear why the $Cu_{1.96}S$ is not reduced further, which suggests that the decomposition process results in domains of $Cu_{1.96}S$, surrounded by Li_2S, so that electrical contact is lost with a significant fraction of this phase.

The mechanisms discussed above occur at two, two-phase interfaces, a mobile anion (F^- in CuF_2) or a Cu^+ ion (in LiCuS), transporting one component of the starting material to the second interface. These mechanisms can allow larger Cu particles to form. The second, important mechanism will occur if Li^+ is the only mobile component, or if Li^+ mobility dominates over Cu^{1+}/Cu^{2+} (or F^-) mobility. Now the reaction has to occur at the triple phase boundary involving the Cu, the lithium salt and the starting material (or intercalation compound). This mechanism is expected to dominate for CuO and as suggested by Li at al., will lead to an LiX:M nanocomposite with very small nanoparticles or amorphous phases.[8] CuO is similar to CuS, in that it forms a limited intercalation phase, which should show some electronic conductivity. However, unlike the CuS system, the Cu mobility in this phase appears to be too slow to allow larger Cu particles to form, with very small 3 nm particles being formed at the end of the discharge process. The Li_xCuO phase should allow at least slow Li^+ diffusion and Li^+ diffusion in Li_2O will also be moderately fast, allowing Li^+ transport through the Li_2O phase to the Li_xCuO/Li_2O/Cu interface. Li^+ diffusion at the grain boundaries may also occur. As illustrated in g and h in Figure 17, small Li_2O and Cu particles should form, because these components are formed simultaneously at the same moving interface. This mechanism will also play a significant role in the CuF_2, particularly at the later stages of the discharge, and to a lesser degree the CuS system, at least near the surfaces of the particles, or if significant Li^+ mobility is possible at the different interfaces so that the Li^+ can reach the triple phase boundary. The mechanism may be enhanced by particle cracking so that the Li^+ transport does not have to occur over such a longer distance. Finally, we note that we have not addressed mechanisms by which additional Li^+ can be stored in these nanocomposites, (i.e., in addition to that based on the capacity associated with the Cu^{2+} to Cu^0 reduction), because all of our electrochemical experiments were arrested above the potential at where this is thought to occur.[8,29] It is clear, however, from this work that the SEI formation (electrolyte decomposition) in these systems appears to be significant, based on our NMR results, and any analysis of additional capacity in these systems will need to take this into account.

5. Conclusion

The different reaction mechanisms by which CuS, CuF_2 and CuO react with Li during the electrochemical process are investigated experimentally. For CuS, at least two insertion phases, Li_xCuS and Li_yCuS (where $0 \leq x \leq 0.16$ and y is close to 1), are observed, a two-phase reaction being observed between the two intercalation phases, in the first stage of the electrochemical reaction. The second process is associated with a conversion reaction of the insertion phase Li_xCuS, as indicated by the observation of Cu metal and Li_2S in significant quantities, after the first plateau, This is consistent with the results of Chung et al.[14] However, unlike these authors, we ascribe the presence of $Cu_{1.96}S$ to the decomposition of LiCuS. A direct conversion reaction mechanism is observed for CuF_2, Cu metal and LiF being seen right at the beginning of discharge. For CuO, the ^{7}Li NMR suggests that an intercalation phase is first formed by ^{7}Li NMR, the CuO tolerating a limited Li content. The particle sizes of the Cu metal formed in CuS are much bigger than those in CuF_2 and CuO based on both the XRD and NMR results. Interestingly though, the Cu particles that first form in the CuF_2 system are much larger. Clearly, the electrochemical reversibility of these copper compounds is not only related to particle sizes of the products formed during the conversion reactions, but both the diffusivity of the different components and the electronic conductivities of the composites play an important role in controlling the electrochemical processes. On the basis of the experimental observations, we suggest a number of mechanisms for the reactions that occur in these systems, involving both triple phase boundaries (e.g., Li_zCuX or CuF_2, Cu and Li_2X or LiF (X=O, S), and in the case of mobile anions F^- or Cu^+, two, two-phase boundaries (Li_zCuX/Cu (or CuF_2/Cu) and Li_zCuX/Li_2X (or CuF_2/LiF)). Clearly, more experimental and theoretical studies are required to determine the relative importance of the different processes, as the reactions progress, but the ideas discussed in this paper provide possible scenarios for the types of reactions that can occur in these classes of materials.

Acknowledgment. The work was supported by the Assistant Secretary for Energy Efficiency and Renewable Energy, Office of FreedomCAR and Vehicle Technologies of the U.S. Department of Energy, under Contract DE-AC03-76SF00098, via Subcontract 6516517749 with the Lawrence Berkeley National Laboratory and by Sony corporation. Use of the APS and the NSLS were supported by the U.S. Department of Energy, Office of Science, Office of Basic Energy Sciences, under Contracts W-31-109-Eng-38 and DE-AC02-98CH10886, respectively. We thank Dr. Jun Wang for collecting data at the APS and Prof. Peter Stephens and Kevin Stone for helping with the XRD data collection at BNL.

Supporting Information Available: Static ^{63}Cu NMR spectra of CuF_2 with 1 and 2.1 Li (Li1.0, Li2.1) and an empty coil (S1). ^{7}Li MAS NMR spectra (at a field strength of 4.7 T) of discharged CuS between Li = 0.45 and Li = v 2.1 and charged CuS between Li = 1.7 and Li = 0.35 (PDF). This material is available free of charge via the Internet at http://pubs.acs.org.